Fracture envelopes on the 3D-DIC and hybrid inverse methods considering loading history

Inje Jang [a,b], Gihyun Bae [a], Junghan Song [a], Haksung Kim [b], Namsu Park [a,*]

[a] Metal Forming Technology R&D Group, Korea Institute of Industrial Technology, 156, Gaetbeol-ro, Yeonsu-gu, Incheon 21999, Republic of Korea
[b] Department of Mechanical Engineering, Hanyang University, Seoul 04763, Republic of Korea

HIGHLIGHTS

- A comparative investigation was performed on the fracture envelopes constructed by the 3D-DIC and hybrid inverse analyses.
- Damage accumulations were numerically studied for the fracture limit transition under non-proportional loading.
- Fracture envelopes on the 3D-DIC and hybrid inverse methods were applied to the simulation of square cup deep drawing.

GRAPHICAL ABSTRACT
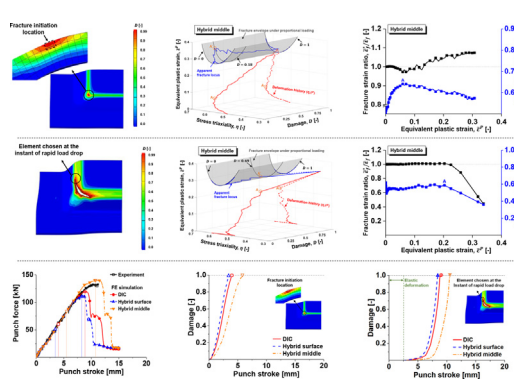
ARTICLE INFO

ABSTRACT

This paper deals with the comparative investigation of fracture envelopes constructed by the 3D-DIC and hybrid inverse analyses. For the evaluation of fracture limits of the DP980 1.2t steel over a wide range of loading conditions, tensile tests were conducted using three different specimens that are expected to induce certain stress states of plane strain tension, in-plane shear, and uniaxial tension at the potential location for the fracture initiation. The modified Mohr–Coulomb ductile fracture criterion was selected in this study to investigate the influence of the fracture envelope identification based on each way of loading history evaluation not only on the level of fracture limits but also on the fracture prediction especially for the simulation of square cup deep drawing. For an in-depth understanding of non-linear loading history on the variation of ductility limit, apparent fracture with respect to strain was numerically computed according to the change of loading path. Finally, a comparison of results from the square cup deep drawing test and the FEA prediction was performed in terms of punch force and stroke to confirm the model performance at various ways of the loading history evaluation.

1. Introduction

In sheet metal forming, necking is considered as the effect before material fracture since the metal sheet is not able to maintain the required strength due to the occurrence of local thinning, ultimately leading to a split in the sheet [1–6]. The Forming Limit Diagram (FLD) based on the necking was, hence, delicately investigated [7,8] for detecting the instant of material instability, which makes possible to reasonably differentiate the safe and failure region in terms of major and minor strain at a wide range of loading paths. Since the FLD is introduced, its application, especially to the automotive industry, is widely accepted so as to predict the forming severity of the sheet metals prior to actual manufacturing. However, as the application of Advanced

Table 1
Mechanical properties of the DP980 1.2t steel sheet.

Loading direction [°]	ε_u [−]	ε_f [−]	w_f/w_0 [−]	l_f/l_0 [−]	Yield stress [MPa]	Ultimate tensile strength [MPa]
0 (RD)	0.101 (±0.008)	0.163 (±0.003)	0.832 (±0.002)	1.163 (±0.003)	719.602 (±2.909)	1005.681 (±1.799)
45 (DD)	0.091 (±0.001)	0.165 (±0.005)	0.776 (±0.001)	1.165 (±0.005)	687.413 (±1.030)	959.201 (±5.380)
90 (TD)	0.081 (±0.005)	0.157 (±0.008)	0.812 (±0.009)	1.157 (±0.008)	722.270 (±26.089)	1010.312 (±25.432)

Table 2
Lankford coefficients according to the angle from the rolling direction.

Loading direction [°]	r-value [−]	$\bar{r}$ [−]	Δr [−]
0 (RD)	0.706 (±0.018)	0.881	−0.025
45 (DD)	0.893 (±0.031)		
90 (TD)	1.031 (±0.065)		

Table 3
Parameters of the Hill's 48 yield function for the DP980 1.2t steel sheet.

F	G	H	N
0.401	0.586	0.414	1.376

High-Strength Steel (AHSS) sheets is significantly increasing for light-weight auto-body, ductile fracture at shear stress components should be followed with great attention as one of the main failure modes in sheet metal forming processes, which cannot be reliably predicted only by necking-based failure criteria.

Ductile fracture refers to the mechanism by which the onset of fracture takes place through the nucleation, growth, and coalescence of microscopic voids in the material. Argon et al. [9] and Goods and Brown [10] argued that void nucleation begins when the interfacial stress reaches a critical value. Rice and Tracey [11] showed that the growth of spherical voids undergoing triaxial tension is directly related to the condition of the stress triaxiality. Weck and Wilkinson [12] proposed two coalescence mechanisms that describe the necking of inter-void

(a)

(b)

(c)
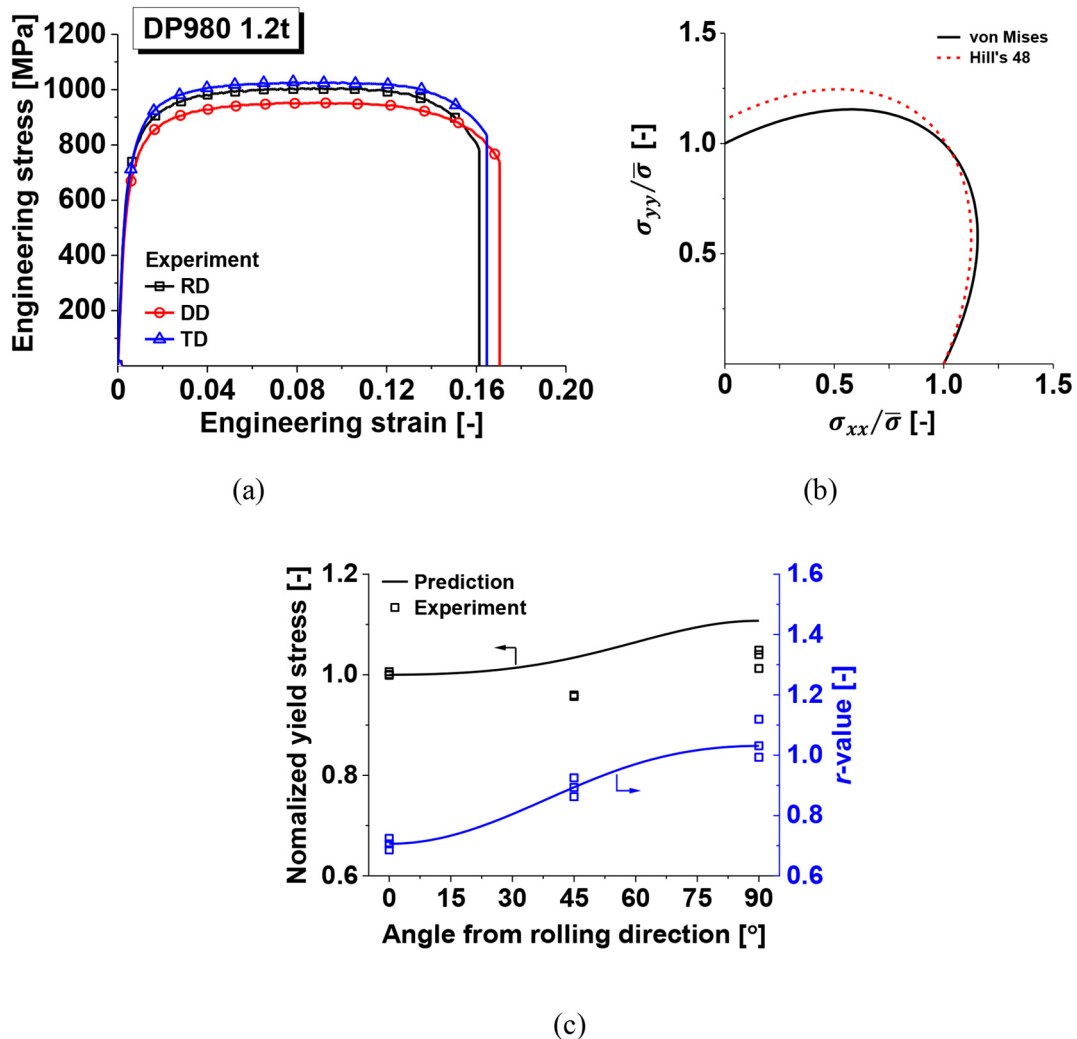
Fig. 1. Results of the DP980 1.2t steel sheet: (a) Engineering stress and engineering strain characteristics; (b) Hill's yield function; and (c) Normalized yield stress and r-value.
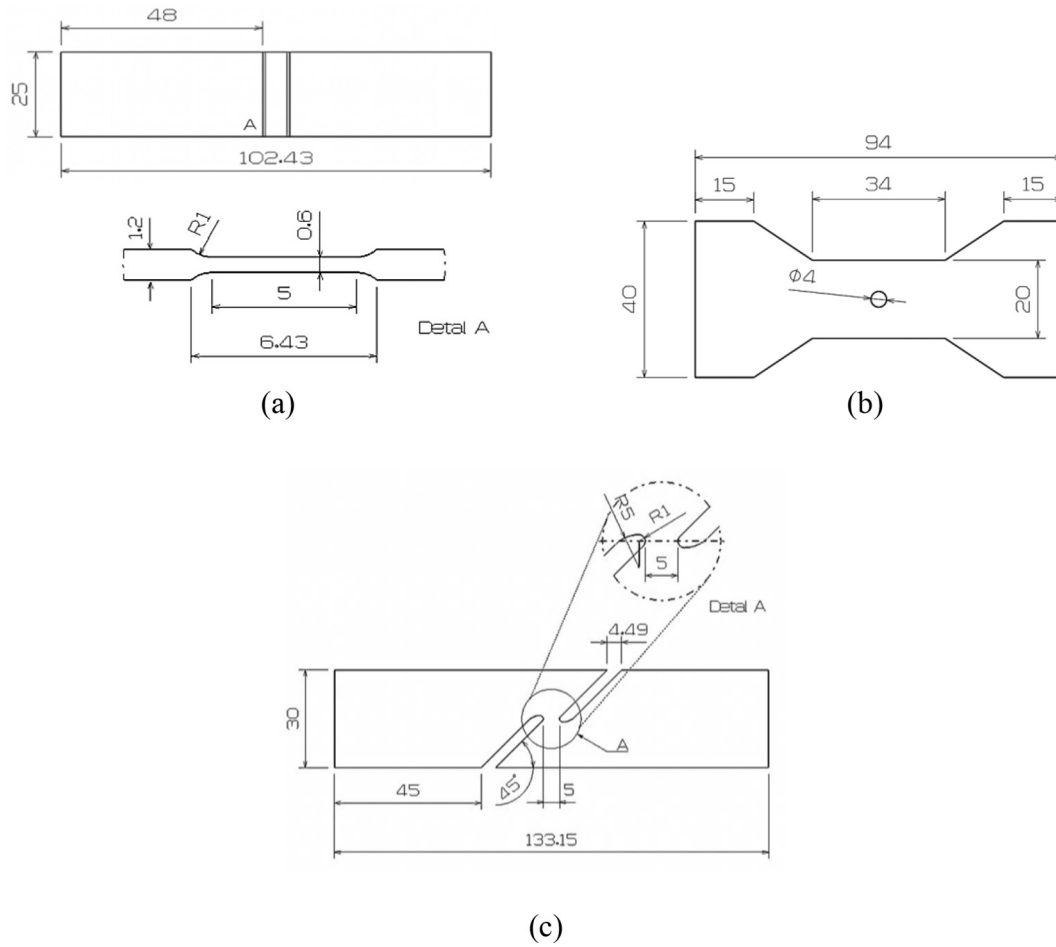
Fig. 2. Specimens of: (a) Plane strain; (b) Center hole; and (c) In-plane shear [unit: mm].
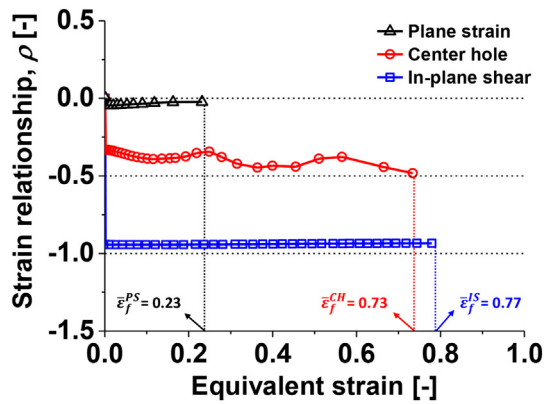
Fig. 3. Relationship between the strain coefficient and equivalent strain determined by the DIC method.

ligaments caused by the maximum principal stress and shear-linking up of voids along the direction of the maximum shear stress. Gurson [13] introduced the nucleation and the growth of voids was mathematically formulated based on porous plasticity. This approach has received considerable attention since Tvergaard and Needleman [14] has incorporated the effect of void coalescence, which is thereafter called the Gurson–Tvergaard–Needlman (GTN) ductile damage model. The GTN model is classified as a coupled damage-plasticity approach since the accumulated damage is represented by the void volume fraction coupled by the constitutive law. Gurson-type models of porous materials have been further extended later to take into account the anisotropy of metal sheets [15]. In the actual deformation process of the material, the physics of damage accumulation and propagation is strongly related to the microstructure of the material and deformation mechanism according to the loading condition as discussed by Chausov et al. [16,17] and Hutsaylyuk et al. [18]. For the investigation of the

Table 4
Information for the finite element analyses.

Young's modulus [GPa]	Poisson's ratio [−]	Total numbers of the elements and the nodes [−]		
		Plane strain tension	Center hole	In-plane shear
200	0.3	33,125/40,824	38,520/47,832	31,585/39,456
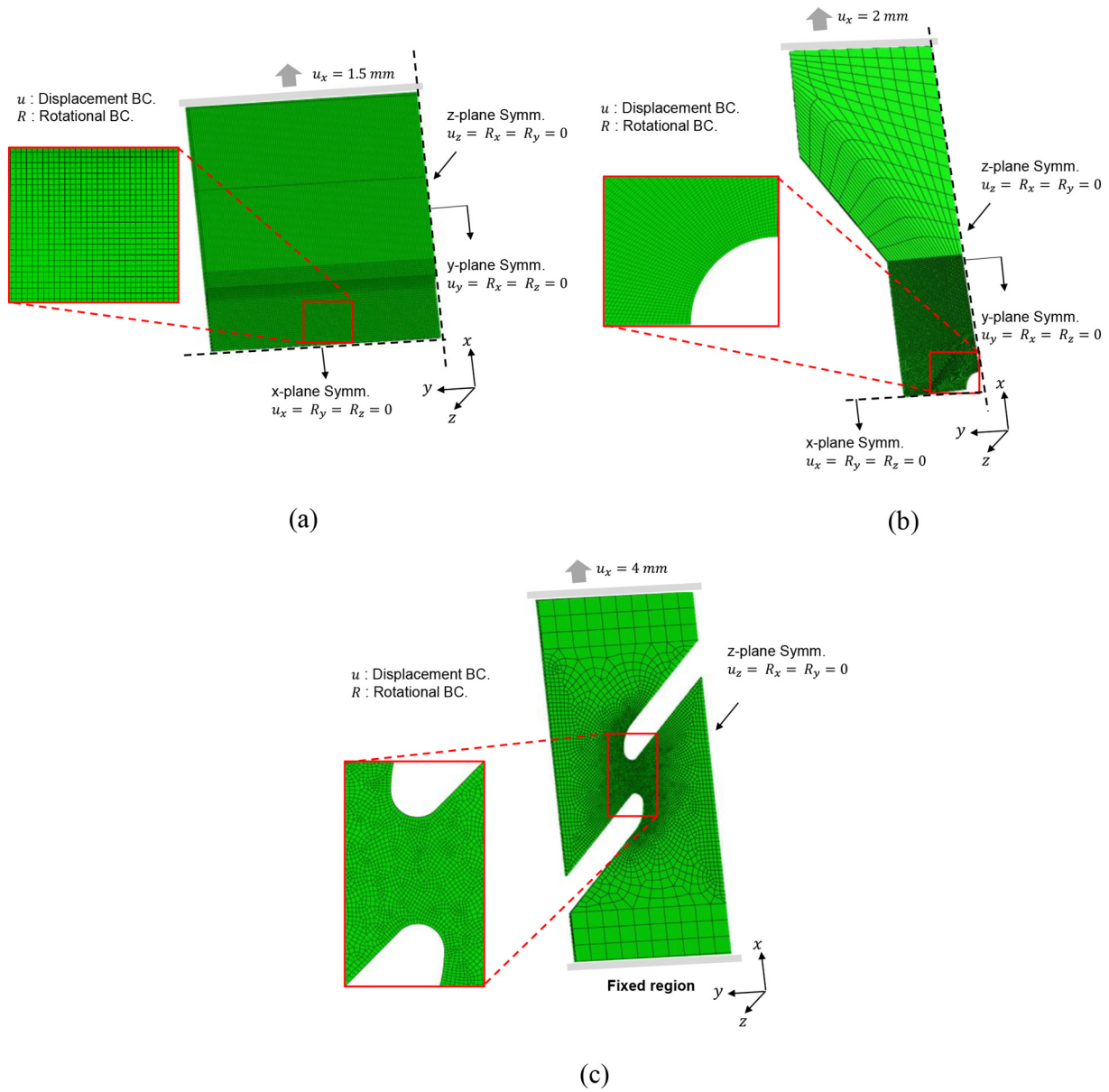
Fig. 4. Finite element models of the tested specimens: (a) Plane strain (a one-eight model); (b) Center hole (a one-eight model); and (c) In-plant shear (a half model).
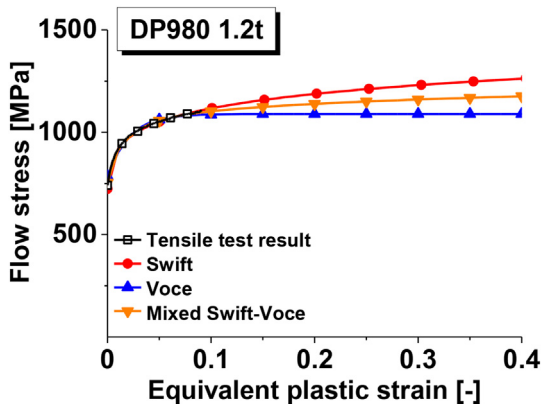
Fig. 5. Flow stress curves of the DP980 1.2t steel sheet used for the finite element analysis.

material fracture kinetics, they proposed a new method of complete stress–strain diagrams that relate material properties to microstructure and damage mechanisms by using experimental data from a complex combined loading mode of Titanium alloy. Although the coupled fracture model and its extended form take into account typical procedures of ductile fracture [19,20], Khan and Liu [21] noted that it is difficult to identify a unique set of the model parameters owing to the strong coupling between them, which may lead to difficulties in its practical application to the industry.

Meanwhile, uncoupled approaches, which ignore the effects of damage accumulation on the strength of metals, can be considered as a suitable candidate for engineering applications [22–25], considering their simplicity and relatively fewer model parameters to calibrate. In general, ductile fracture criteria based on the uncoupled approach predicts the onset of fracture when the integral of plastic deformation multiplied by a weighting function that considers the state of stress reaches a critical value. Various forms of the weighting functions are accordingly proposed in last decades to develop the fracture criterion that provides reasonable accuracy for its practical application for engineering
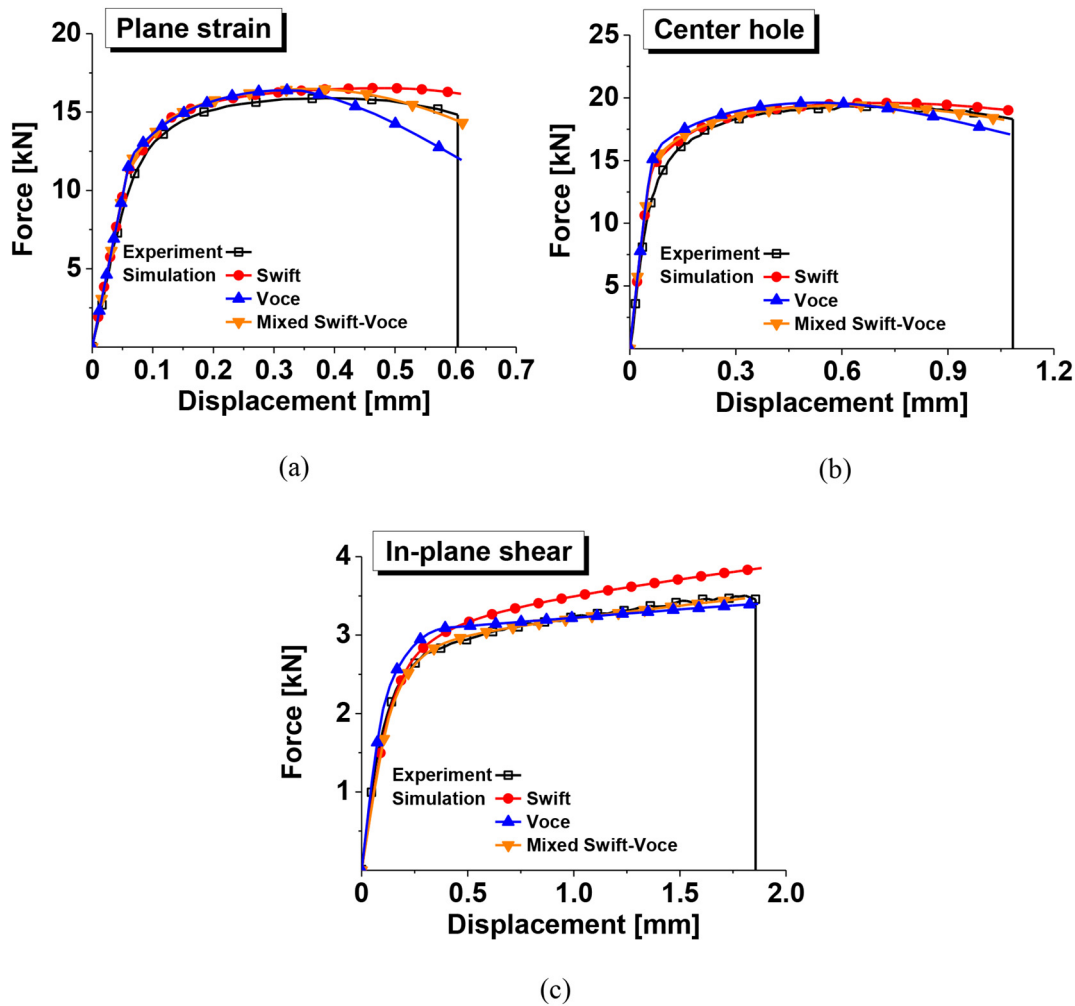
Fig. 6. Comparison between the tensile force–displacement curves evaluated from the tests and the finite element analyses: (a) Plane strain; (b) Center hole; and (c) In-plane shear. Note that the experimental results were captured using MTS 810 testing machine and the 3D-DIC system.

Table 5
Parameters of the mixed Swift–Voce strain hardening law for the DP980 1.2t steel sheet.

Loading direction [°]	Swift strain hardening law			Voce strain hardening law			Weight
	K [MPa]	ε_0 [−]	n [−]	A [MPa]	B [MPa]	C [−]	λ [−]
0 (RD)	1367.907	0.000731	0.08827	1089.379	304.966	47.890	0.500

problems. McClintock et al. [26] proposed the weighting function based on the analytical investigation on the growth of a cylindrical void. LeRoy et al. [27] observed from the void growth and damage accumulation during tensile that the maximum principal and hydrostatic stresses are crucial factors to deal with the fracture initiation. Cockcroft and Latham [28] employed the maximum principal stress to define the weighting function, and later Oh et al. [29] considered the normalized maximum principal stress to predict the ductile fracture during the extrusion process for AA2024-T351. Brozzo et al. [30] further added a hydrostatic stress term for the purpose of improving the model performance.

A wealth of literature regarding the uncoupled modeling approach revealed limitations of the previous fracture model defined in terms of the stress triaxiality especially in predicting the onset of fracture that depends on the normalized third invariant of the deviatoric stress tensor. In a consequence, extensive efforts are put into developing the

generalized fracture model that is capable of describing the asymmetric fracture limit in reference to the generalized shear state, i.e., $(\sigma_1, \frac{\sigma_1+\sigma_3}{2}, \sigma_3)$ where the principal stresses are in the order of $\sigma_1 \geq \sigma_2 \geq \sigma_3$. Wilkins et al. [31] studied the influence of Lode angle associated with the third invariant of deviatoric stress tensor on the fracture initiation. Simultaneously, the Lode dependence of ductile fracture was confirmed from a series of combined torsion–tension experiments [32–34]. Xue and Wierzbicki [35] stressed the necessity of including the mutual effect of the stress triaxiality and the Lode angle for reliable prediction of both deformation and fracture behaviors. Bai and Weirzbicki [36] further showed from extensive fracture tests that the material ductility can be significantly affected by changes in the Lode angle, especially where the stress state is under the shear-dominated loading condition. Later, Bai and Weirzbicki [37] extended the Mohr–Coulomb (M–C) criterion to ductile fracture and represented the fracture limit in terms of the equivalent strain, the stress triaxiality, and the Lode angle parameter. In addition, Bai and Wierzbicki [38] calibrated and evaluated fracture loci of sixteen fracture models by classifying into three types of physical-based, phenomenological, and empirical models. Jia and Bai [39] developed the all-strain-based modified M–C model using a linear transformation approach to predict anisotropic fracture initiation of sheet metal.

For the reliable prediction of fracture initiation, the phenomenological fracture criterion is needed to be identified by a certain set of experimental data that cover a broad range of stress states [40–43]. Bao and
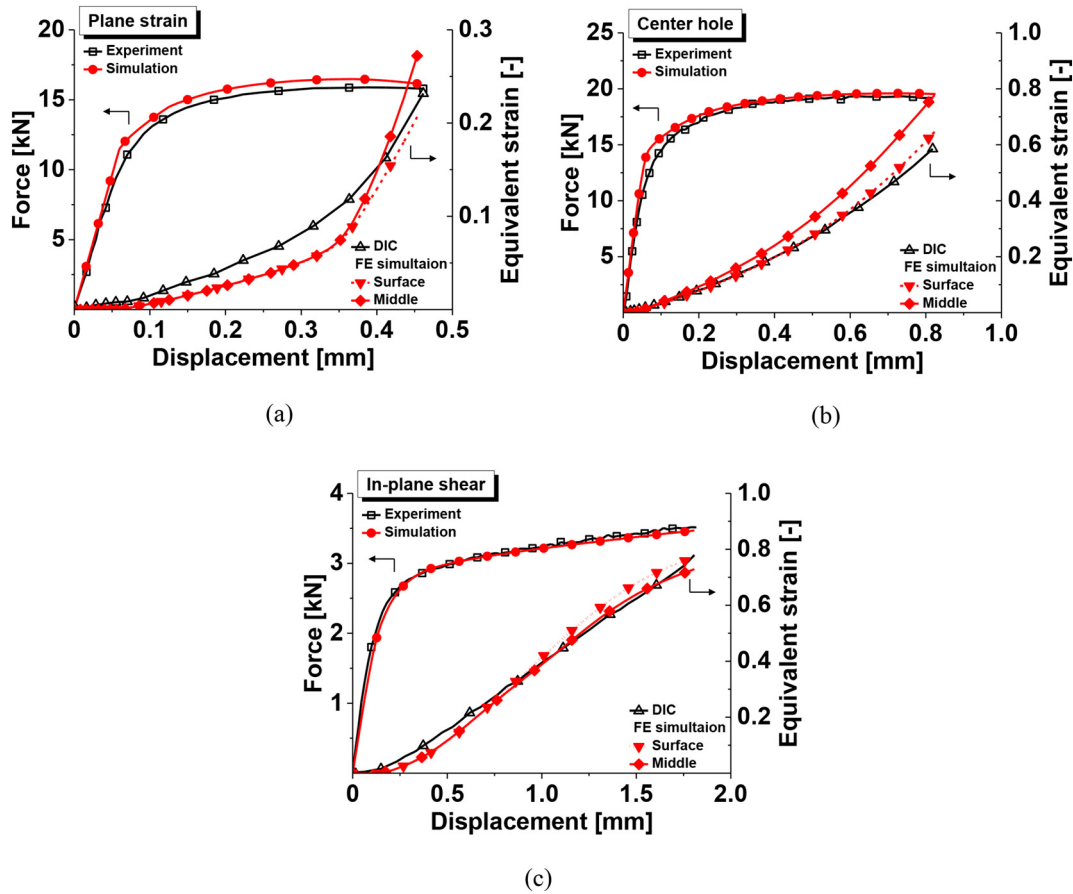
Fig. 7. Force and equivalent strain histories evaluated from the tests and the finite element analyses: (a) Plane strain; (b) Center hole; and (c) In-plane shear.

Weirzbicki [44] and Beese et al. [45] designed various shapes of specimens for the fracture test to induce a typical loading state until the fracture initiates. In an attempt to estimate the localized fracture strain over a broad range of stress triaxiality from uniaxial tension to equi-biaxial tension, Dunand and Mohr [46] introduced a hybrid inverse analysis which compares the results between the tensile test and the numerical analysis in terms of the force history and the strain distribution on the surface of a test sample. Lou and Yoon [47] experimentally analyzed the effect of anisotropy in the fracture behavior of AA6k21 sheet. Charoensuk et al. [48] predicted damage accumulation and fracture initiation of advanced high strength steel sheets considering the effects of anisotropy based on the direct current potential drop method. Lou and Yoon [49] employed the form of Drucker yield function to model the anisotropic fracture behavior of AA2024-T351 based on two distinct linear transformation tensors. Recently, Park et al. [50] proposed a decoupled formulation using the Lagrangian interpolation function to deal with the fracture prediction considering general anisotropy of metal sheets. The damage form of the uncoupled fracture criterion brings about the issue of non-uniqueness of fracture limit: i.e., the fracture limit can vary according to the loading history that the material experiences during the deformation, which is needed to be carefully investigated.

In this study, a comparative investigation are carried out concerning the identification of the phenomenological fracture criterion with the use of the strain data evaluated from the 3D-DIC and hybrid inverse analyses. The tensile tests of the DP980 1.2t (DP980 with the thickness of 1.2 mm) steel sheet were conducted using three different types of specimens to evaluate the deformation at certain stress states, i.e., plane strain, in-plane shear, and uniaxial tension. For the quantitative investigation of the influence of limit strains on the fracture,

fracture envelopes constructed by the 3D-DIC and hybrid inverse analyses were applied to the simulation of square cup deep drawing and the predictions were compared to the experimental data in terms of punch loading and stroke. Finally, damage accumulations for each case were numerically studied for an in-depth understanding of the fracture limit transition under non-proportional loading history.

2. The DP980 1.2t steel in mechanical tests

In this paper, the mechanical characteristic of DP980 1.2t steel was analyzed. The DP980 1.2t steel in a form of sheet is typically used in applications requiring high strength and adequate formability, such as structural and crashworthiness parts including B-pillar, floor panel tunnel, engine cradle, and front sub-frame package tray of auto body. For the material characterization, a tensile test of the DP980 1.2t steel sheet was carried out by means of the MTS 810 testing machine. The commercial software of ARAMIS v6.1.0 was used to measure not only the strain distribution but also the localized strain on the measuring zone of specimens that were prepared according to the ASTM E8M standard capturing a gauge length of 25 mm. It is noted that, for evaluation of the anisotropy characteristic, the specimens were selected from the following directions of 0° (Rolling Direction, RD), 45° (Diagonal Direction, DD), and 90° (Transverse Direction, TD). Tables 1 and 2 list the anisotropic mechanical properties obtained under the quasi-static loading condition with a constant crosshead velocity of 0.025 mm/s. Note that, in Table 1, w_f and l_f indicate the transverse and longitudinal elongations of the specimen at fracture, respectively.

In order to take into account the anisotropy of mechanical properties, the Hill's yielding function for biaxial stress state, as given in Eq. (1), is considered. The model parameters calibrated by the r-values
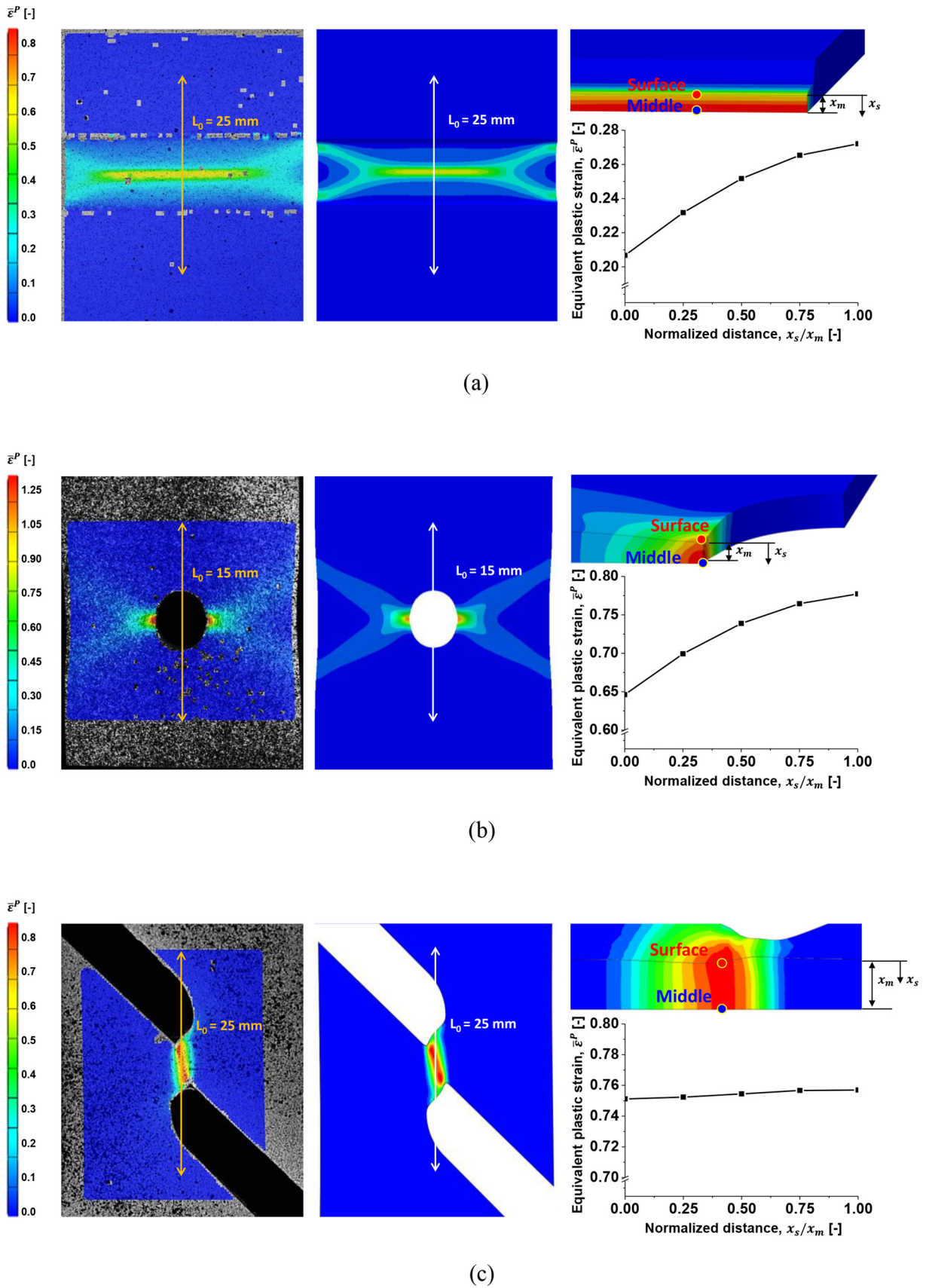
Fig. 8. Comparison of the equivalent strain distribution from the tests and the finite element analyses before fracture: (a) Plane strain; (b) Center hole; and (c) In-plane shear.
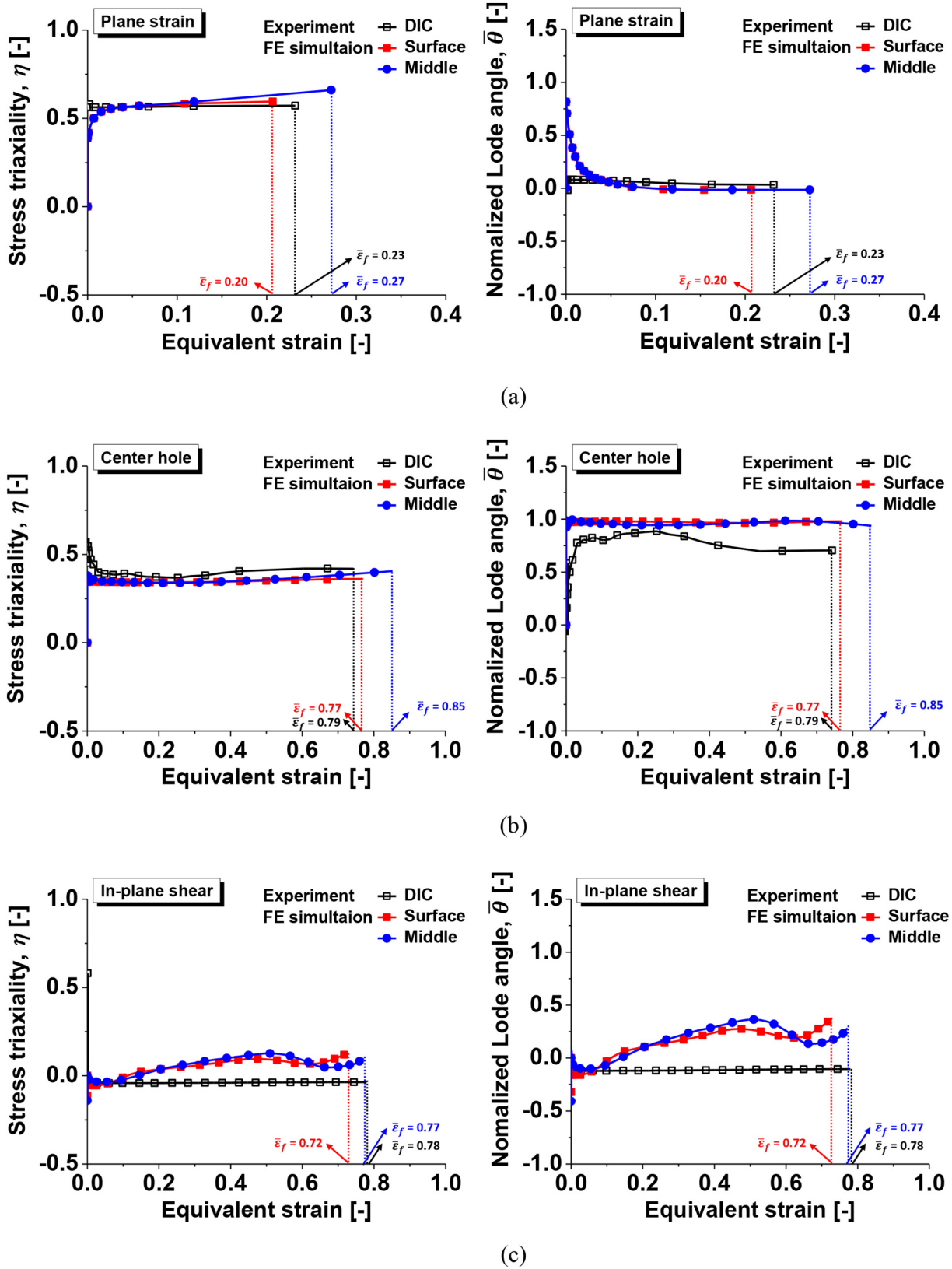
Fig. 9. Evolution of the stress triaxiality and the normalized Lode angle evaluated from the tests and the finite element analyses: (a) Plane strain; (b) Center hole; and (c) In-plane shear.

Table 6
Parameters of the modified Mohr–Coulomb fracture criterion.

Fracture evaluation method	C_1 [−]	C_2 [MPa]	C_3 [−]
3D-DIC analysis (on the surface of a specimen)	0.101	739.797	0.964
Hybrid inverse analysis (top layer)	0.143	769.867	0.971
Hybrid inverse analysis (middle layer)	0.586	748.692	0.961

are listed in Table 3, and the corresponding yield locus is represented in Fig. 1 with the anisotropic strain hardening response.

$$\overline{\sigma} = \sqrt{(G+H)\sigma_{xx}^2 - 2H\sigma_{xx}\sigma_{yy} + (H+F)\sigma_{yy}^2 + 2N\sigma_{xy}^2}$$ (1)

where F, G, H, and N are the material parameters defined as:

$$F = \frac{r_0}{\sigma_0^2(1+r_0)r_{90}}, G = \frac{1}{\sigma_0^2(1+r_0)}, H = \frac{r_0}{\sigma_0^2(1+r_0)}, N$$
$$= \frac{(2r_{45}+1)(r_0+r_{90})}{2\sigma_0^2(1+r_0)r_{90}}$$ (2)

3. Evaluation of the equivalent strain to fracture

3.1. 3D-DIC analysis

Specimens for the fracture tests were machined as shown in Fig. 2, concerning the stress states of in-plane shear, uniaxial tension, and plane strain tension at each location where the fracture initiation is expected. The equivalent strain distribution and the localized strain were measured by means of the 3D-DIC system. Note that the spatial resolution and frame rate used were around 0.01 mm/pixel and 5 fps, respectively.

Fig. 3 shows the variations of major and minor relationship versus equivalent strain at each fracture location until the onset of fracture takes place. Here, the strain relationship is defined as the ratio of the major to minor strain increments, i.e., $\rho = d\varepsilon_2/d\varepsilon_1$. For the isotropic material, the theoretical values of the strain coefficient ρ for in-plane shear, uniaxial tension, and plane strain tension are −1, −0.5, and 0, respectively. Considering the strain relationship almost constant during each test, it can be concluded that the equivalent stress at fracture is strongly related to material type and its mechanical properties as well as features of the strain proportion.
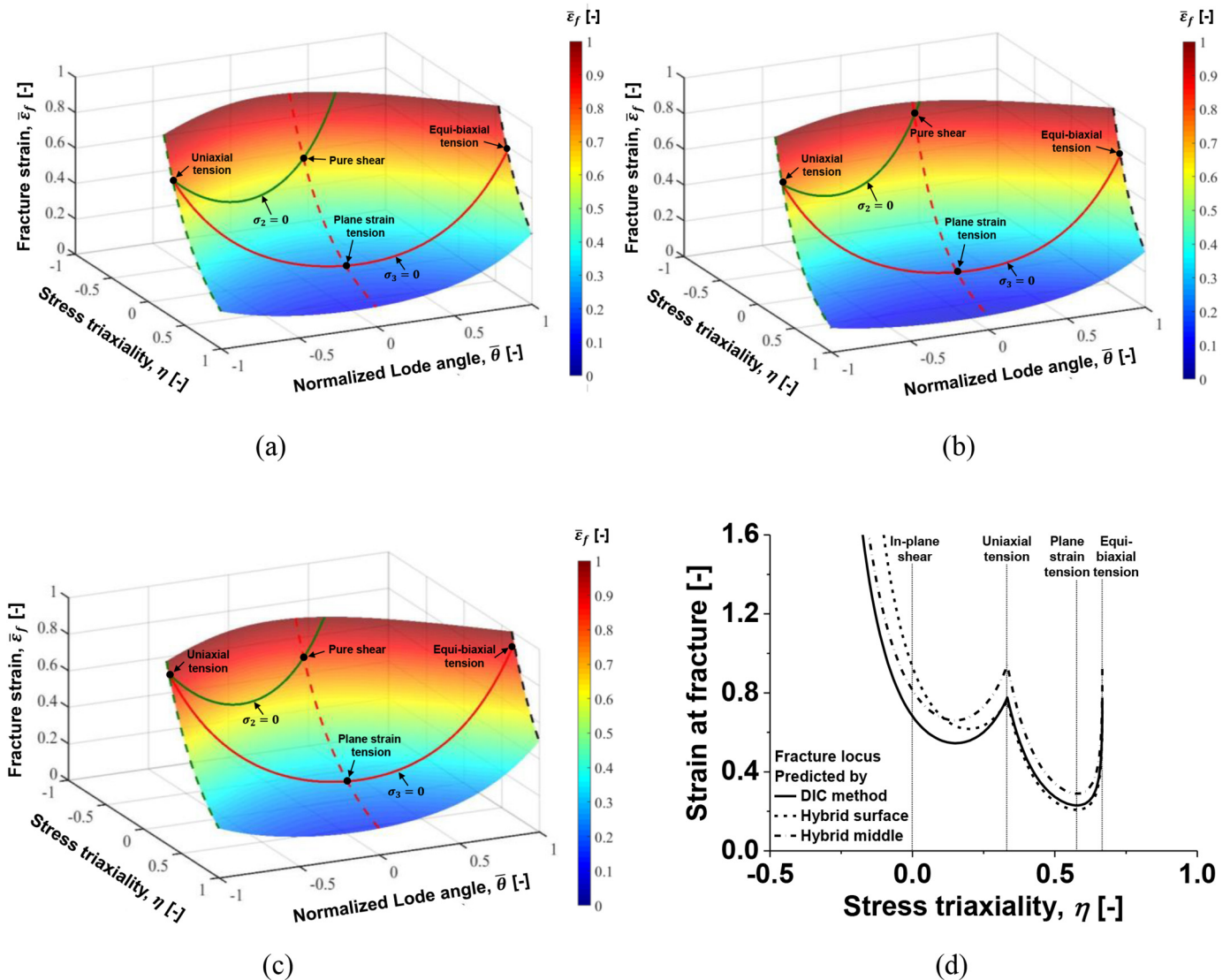
Fig. 10. Fracture envelopes calibrated for each loading types: (a) the 3D-DIC analysis; and the hybrid inverse analysis using the data obtained from (b) the top and (c) the middle layers; and (d) Comparison of the fracture loci constructed.
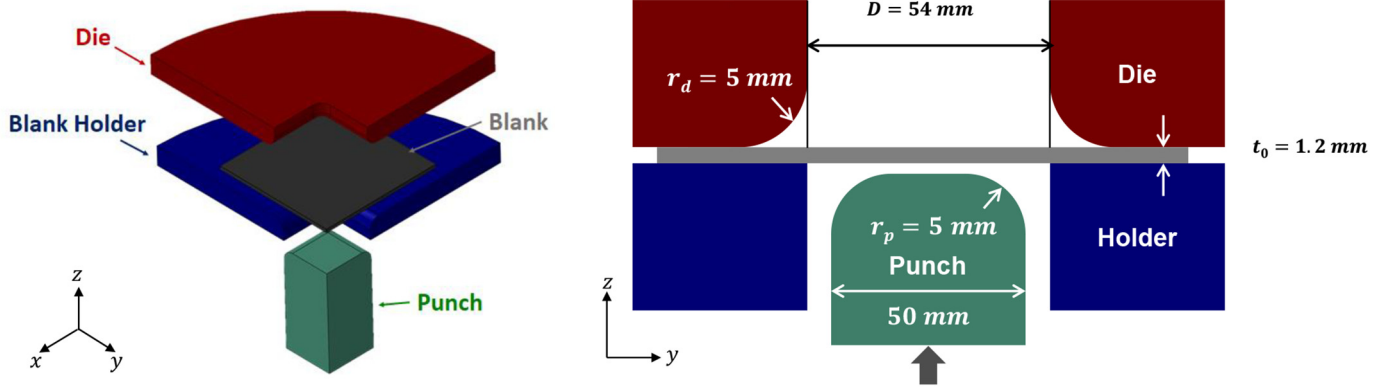
Fig. 11. A scheme of the square cup deep drawing.

Fig. 12. Fracture region from the test and the finite element analysis.

3.2. Hybrid inverse analysis

As a way of numerical approximation, a hybrid inverse analysis [46] was employed in this study for the evaluation of histories of the stress state and equivalent strain until the fracture initiates. All the Finite Element (FE) simulations were conducted in the environment of ABAQUS/ Implicit v6.14. The element type of reduced-integration eight-node 3D solid was used to mesh the FE region of each specimen. An element edge length of about 0.1 mm was assigned, and five element layers were made through the half-thickness around the primary deformation area for each FE model. The brief information for the numerical analyses is summarized in Table 4. Each FE model with the boundary conditions is illustrated in Fig. 4. It is noted that a one-eight model was considered in the FE simulations except for the shear case in order to reduce the computational cost. The Hill's yield function was applied to take into consideration of the anisotropy of mechanical properties at the numerical analyses. Fig. 5 shows the three different flow curves fitted by the Swift (k_S), Voce (k_V), and mixed Swift–Voce (k_M) hardening laws employed in the FE analyses to validate the applicability of each flow curve at large plastic deformation for the reliable fracture analysis that normally involves a high level of strain localization at the fracture site. By comparing force and displacement curves evaluated from the tests and the FE simulations as shown in Fig. 6, it is confirmed that the flow curve fitted by the mixed Swift–Voce hardening law has superiority in describing the deformation behavior. Note that the mixed Swift–Voce hardening law is defined as a linear combination of the Swift and Voce hardening laws with a weight term of λ:

$$k_M = \lambda k_S + (1-\lambda)k_V \tag{3}$$

where

$$k_S = K(\varepsilon_0 + \bar{\varepsilon}^p)^n, k_V = A + B\left(1-e^{-C\bar{\varepsilon}^p}\right) \tag{4}$$

The model parameters calibrated are summarized in Table 5. In the hybrid inverse analyses, comparisons between the tests and the FE simulations for each case were performed in terms of not only the force and equivalent strain histories but also the strain distribution before the fracture initiation as shown in Figs. 7 and 8. Since the predictions show excellent agreements with the test results, the state variables including the Cauchy stress and strain tensors predicted can be considered as close measures of actual physical quantities for the deformed specimen. Strain localization accompanied by the necking was observed during the tests especially for the loading cases of plane strain tension and uniaxial tension. In the deformation concentrated area, the equivalent plastic strain evaluated tends to increase from the surface to the middle layers of the sample due to the generation of triaxial stress states, as is not the case for in-plane shear.

4. Prediction of the fracture limit

4.1. Evaluation of the loading history

For the calibration of the uncoupled ductile fracture criterion, it is necessary to obtain the histories of the stress triaxiality η and the normalized Lode angle $\bar{\theta}$ whose combination represents a certain loading condition. Each stress invariant is theoretically defined as: $\eta = \sigma_m/\bar{\sigma}$ and $\bar{\theta} = 1-(2/\pi)\cos^{-1}\left(27J_3/2\bar{\sigma}^3\right)$. Since the internal stress state of the test specimen is not able to be directly obtained by the DIC analysis, the stress was estimated by a theoretical relationship between the strain and stress based on the associated flow rule, i.e., $d\varepsilon_{ij}^p = d\bar{\varepsilon}^p \partial\bar{\sigma}/\partial\sigma_{ij}$. From a simple mathematical manipulation with the Hill's yield function, the stress proportion α is defined in terms of the strain relationship ρ as below:

$$\alpha = \frac{\sigma_2}{\sigma_1} = \frac{(G+H)\rho + H}{H\rho + H + F} \tag{5}$$

Accordingly, the stress triaxiality and the normalized Lode angle can be expressed by the strain relationship under the plane stress assumption:
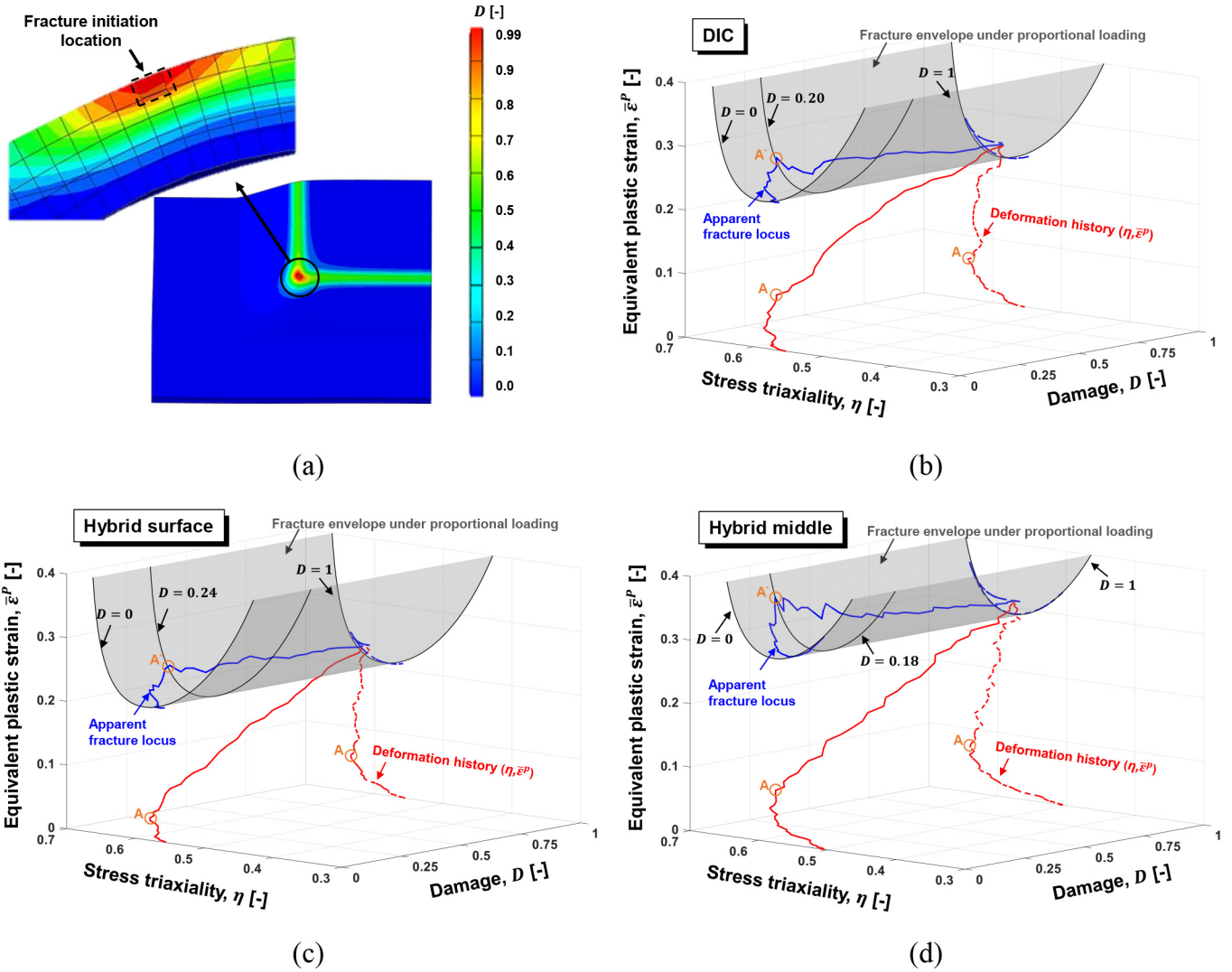
Fig. 13. Variation of the strain at fracture according to the deformation history extracted from the element firstly deleted: (a) the location of fracture initiation; and the change of ductility in conjunction with the fracture locus calibrated from (b) the 3D-DIC analysis; and the hybrid inverse analysis using the data obtained from (c) the top and (d) the middle layers.

$$\eta = \frac{1+\alpha}{3\sqrt{1-\alpha+\alpha^2}}, \bar{\theta} = 1 - \frac{2}{\pi}\cos^{-1}\left[-\frac{27}{2}\eta\left(\eta^2 - \frac{1}{3}\right)\right] \tag{6}$$

Fig. 9 shows the evolution of the above stress invariants evaluated from the 3D-DIC and the hybrid inverse analyses, which will be further used for the calibration of fracture envelope to predict the limit strain at fracture.

4.2. Construction of fracture envelopes based on the DIC and hybrid inverse analyses

The Modified Mohr–Coulomb (MM–C) criterion [37] was employed for the prediction of fracture limits over a wide range of loading conditions:

$$\bar{\varepsilon}_f(\eta,\bar{\theta}) = \left\{\frac{A}{c_2}\left[1 - c_\eta(\eta - \eta_0)\right]\left[c_\theta^s + \frac{\sqrt{3}}{2-\sqrt{3}}(c_\theta^{ax} - c_\theta^s)\left(\sec\frac{\bar{\theta}\pi}{6} - 1\right)\right]\right.$$

$$\left.\left[\sqrt{\frac{1+c_1^2}{3}}\cos\frac{\bar{\theta}\pi}{6} + c_1\left(\eta + \frac{1}{3}\sin\frac{\bar{\theta}\pi}{6}\right)\right]\right\}^{-1/n} \tag{7}$$

Basically, the eight parameters ($A, n, c_\eta, \eta_0, c_\theta^s, c_\theta^c, c_1, c_2$) are required to be calibrated for the construction of the fracture envelope from the

MM–C criterion. It is noted that the MM–C criterion is sort of the uncoupled phenomenological fracture modeling approach so that it is not able to describe changes of the microstructure and its influences on the physical damage mechanism [18]. The MM–C criterion can be reduced to the one with the three parameters (C_1, C_2, C_3) for the sake of simplicity by neglecting the terms related to the pressure sensitivity on yield surfaces and the asymmetry of the fracture envelope. The reduced MM–C criterion has a form of

$$\bar{\varepsilon}_f(\eta,\bar{\theta}) = \left\{\frac{A}{C_2}\left[C_3 + \frac{\sqrt{3}}{2-\sqrt{3}}(1-C_3)\left(\sec\frac{\bar{\theta}\pi}{6} - 1\right)\right]\right.$$

$$\left.\left[\sqrt{\frac{1+C_1^2}{3}}\cos\frac{\bar{\theta}\pi}{6} + C_1\left(\eta + \frac{1}{3}\sin\frac{\bar{\theta}\pi}{6}\right)\right]\right\}^{-1/n} \tag{8}$$

Here, C_1, C_2, and C_3 represent a friction coefficient, shear resistance of the Mohr–Coulomb fracture model, and a coefficient related to the Lode angle dependence on fracture, respectively. The fracture criterion defined above describes the equivalent strain at fracture assuming the proportional (or linear) loading path, which means that it would be inappropriate to directly apply it as a limit to deal with the fracture initiation in forming processes accompanying non-linear loading history,
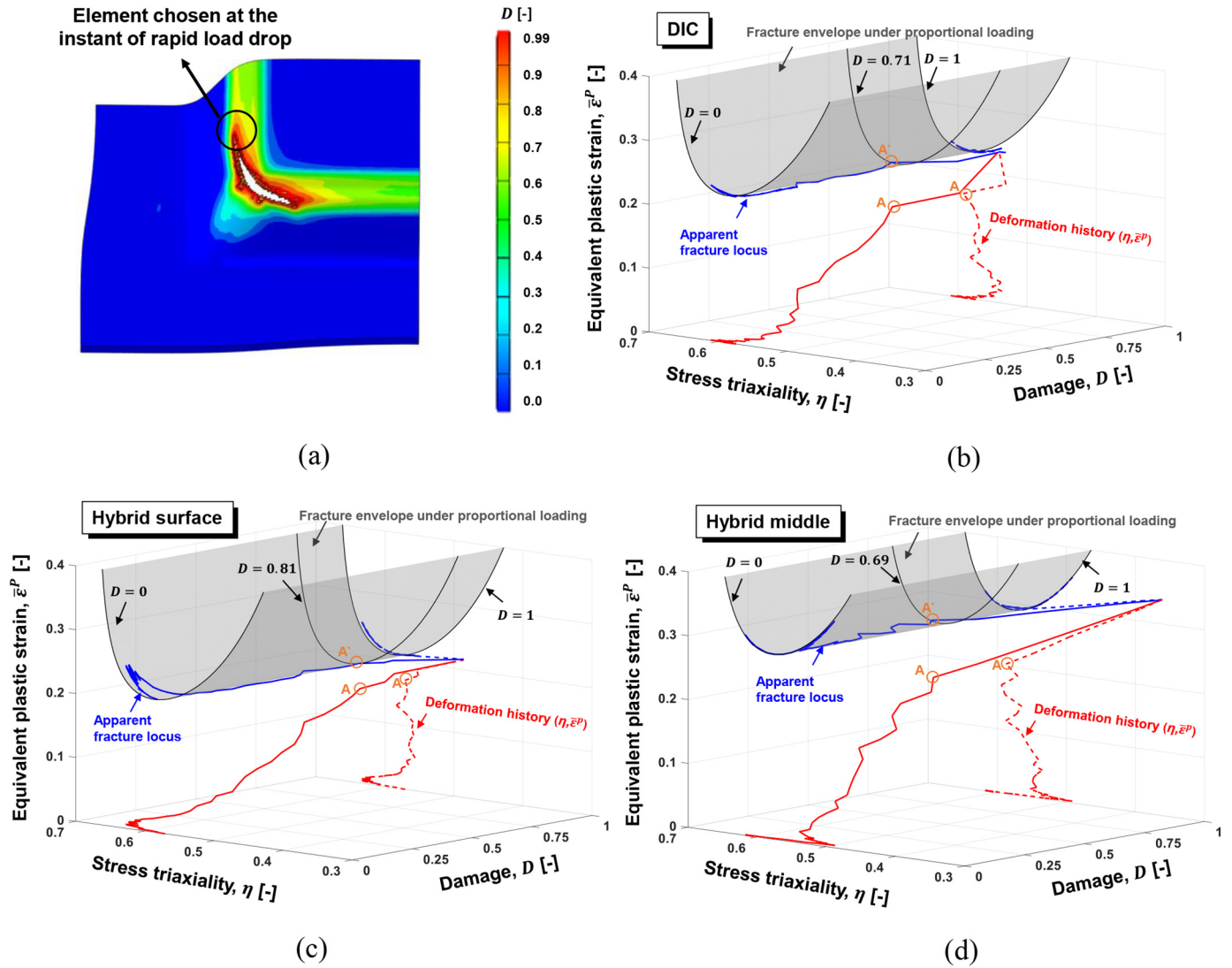
Fig. 14. Variation of the strain at fracture according to the deformation history extracted from the element deleted at the instant of rapid load drop: (a) the location of fracture initiation; and the change of ductility in conjunction with the fracture locus calibrated from (b) the 3D-DIC analysis; and the hybrid inverse analysis using the data obtained from (c) the top and (d) the middle layers.

e.g., multi-stage forming process, during the deformation of the workpiece. For the consideration of the effect of loading history on the fracture initiation, a damage accumulation law of $D = \int \frac{d\bar{\varepsilon}^p}{\bar{\varepsilon}_f(\eta,\bar{\theta})}$ was adopted in this study, which takes into account of changes in the stress state in an integral form. Here, the damage index $D \in [0,1]$ is related to the residual ductility of the material until the fracture initiation. Numerically, the onset of fracture takes place as D reaches unity.

The model parameters given in Table 6 were identified by solving the optimization problem of

$$\min_{C_i} \sum_{j=1}^{3} \left| 1 - D_j\left(\eta, \bar{\theta}, \bar{\varepsilon}^p\right) \right| \tag{9}$$

where the subscript j stands for the typical loading condition for the fracture test such as in-plane shear, uniaxial tension, and plane strain tension. Each fracture envelope was calibrated with the use of the stress and strain evaluated from the 3D-DIC and hybrid inverse analyses. Fig. 10 represents the 3D fracture envelopes and their corresponding 2D fracture loci extracted under the plane stress assumption. It was confirmed from the predictions that, in the tension-dominated loading state, both measuring ways of the loading history provide almost the

same level of fracture limits predicted from the surface layer while deviations arise in the shear-dominated region due to differences between the loading histories of in-plane shear used for the calibration of fracture envelope. It is worth to note that one can expect to have a more reliable set of material parameters for the fracture criterion if the parameters are calibrated with the use of the stress and strain history from the FEA prediction based on the advanced plasticity model such as evolutionary anisotropy, kinematic hardening, etc., which allows to describe the material yielding in a more accurate manner.

5. Prediction of the fracture initiation under square cup deep drawing

For the purpose of investigation of the model performance on the fracture initiation, a square cup deep drawing test of the DP980 1.2t steel sheet was conducted with the blank size of 90 mm × 90 mm, assigning the punch velocity of 1 mm/s and the blank holding force of 180 kN, considering the quasi-static loading condition. The corresponding numerical analysis was performed by means of the commercial FE software of ABAQUS v6.14. The blank was discretized with five element layers through the thickness, using the reduced-integration
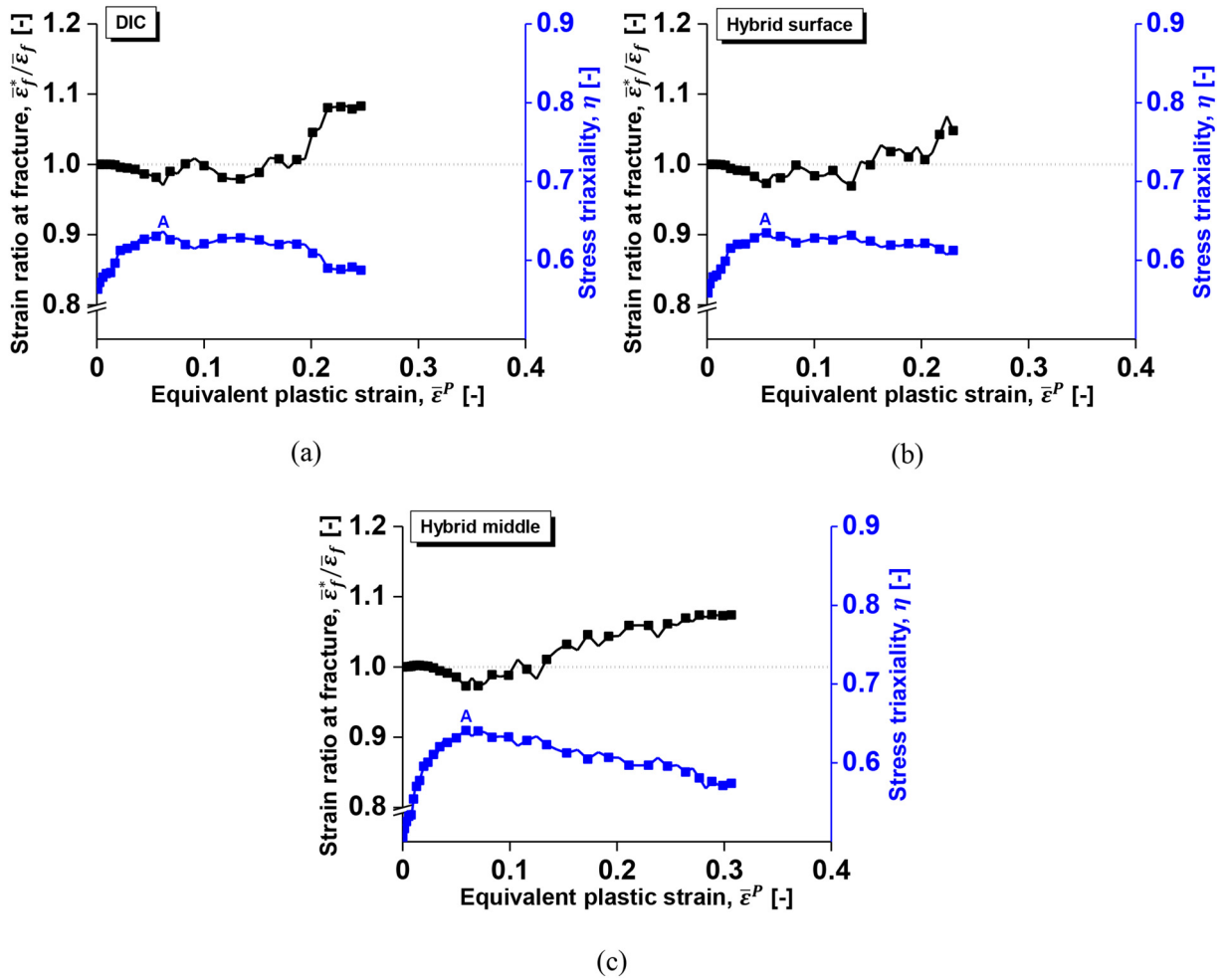
Fig. 15. Variations of the strain ratio to fracture and the stress triaxiality extracted at the element firstly deleted for each square cup drawing simulation employing the fracture locus calibrated from: (a) the 3D-DIC analysis; and the hybrid inverse analysis using the data obtained from (b) the top and (c) the middle layers.

eight-node 3D solid element with an edge length of about 0.1 mm. The punch, die, and blank holder were modeled as rigid bodies, and the friction coefficient of 0.1 was assigned between contact areas for matching up with the punch force histories between the test and the FE analysis. With the aim of reducing computational cost, a quarter FE model was developed in the numerical simulation as illustrated in Fig. 11. In the numerical analysis, the plastic deformation and hardening were described by the Hill's yield function and the mixed Swift–Voce strain hardening law discussed in Section 3.2.

Fig. 12 represents the comparison of the test result and the prediction from the FE analysis, showing good agreements in terms of the fracture location. The deformation history predicted at the fracture location revealed that the material point mainly undergoes near the loading state of plane strain tension prior to the fracture initiation as shown in Fig. 13. It is worthwhile to mention that each fracture envelope applied in the FE analyses was constructed with the postulate of proportional loading path. Considering the integral form of the fracture criterion, i.e., $D = \int \frac{\mathrm{d}\bar{\varepsilon}^p}{\bar{\varepsilon}_f(\eta,\bar{\theta})}$, the equivalent strain at fracture is, however, not a constant but a changeable quantity dependent on the loading history that the material undergoes until the fracture initiation, which implies that the fracture limit varies according to the loading history experienced during the deformation, and hence one may misinterpret this dynamic feature of the fracture envelope, especially for the case when it is graphically represented together with results for the non-linear loading history of the fractured element. For an in-depth understanding of the

dynamic characteristic of the fracture envelope particularly on the change of material ductility in conjunction with the damage accumulation through the entire loading history, the variation of equivalent plastic strain to fracture was numerically investigated by evaluating the so-called apparent fracture strain discussed by Chung et al. [51]. In order to reflect influence of the effect due to loading history on the variation of fracture strain, the fracture limit predicted under proportional loading is consecutively adjusted by not only the accumulated equivalent plastic strain but also its corresponding damage increment with the progress of deformation, considering the relative values of damage level computed at the previous, $n - 1$, and current, n, time stages, i.e.,

$$\bar{\varepsilon}_f^* \eta_n = \sum_{i=1}^{n-1} \Delta \bar{\varepsilon} \eta_i + \bar{\varepsilon}_f \eta_n \cdot 1 - \sum_{i=1}^{n-1} \Delta D_i \tag{10}$$

or, equivalently,

$$\bar{\varepsilon}_f^* \eta = \int \mathrm{d}\bar{\varepsilon}^p + \bar{\varepsilon}_f \eta \cdot 1 - D = \bar{\varepsilon}_f \eta + \int \mathrm{d}\bar{\varepsilon}^p - \bar{\varepsilon}_f \eta \cdot D \tag{11}$$

where $\bar{\varepsilon}_f^*(\eta)$ and $\bar{\varepsilon}_f(\eta)$ denote the strain at fracture depended on the change of loading path and the strain to fracture under proportional loading, respectively. Here, the quantity, $\int \mathrm{d}\varepsilon - \varepsilon_f(\eta) \cdot D$, reflects the effect of the deformation history on the fracture: e.g., for $\eta_n > \eta_{n-1}$, $\bar{\varepsilon}_f^*(\eta_n)$ N$\bar{\varepsilon}_f(\eta_n)$ when $D(\eta_n) > D(\eta_{n-1})$, and $\bar{\varepsilon}_f^*(\eta_n)$ b$\bar{\varepsilon}_f(\eta_n)$ when $D(\eta_n) < D(\eta_{n-1})$. For the state in which there is no path change during the

(a)

(b)

(c)
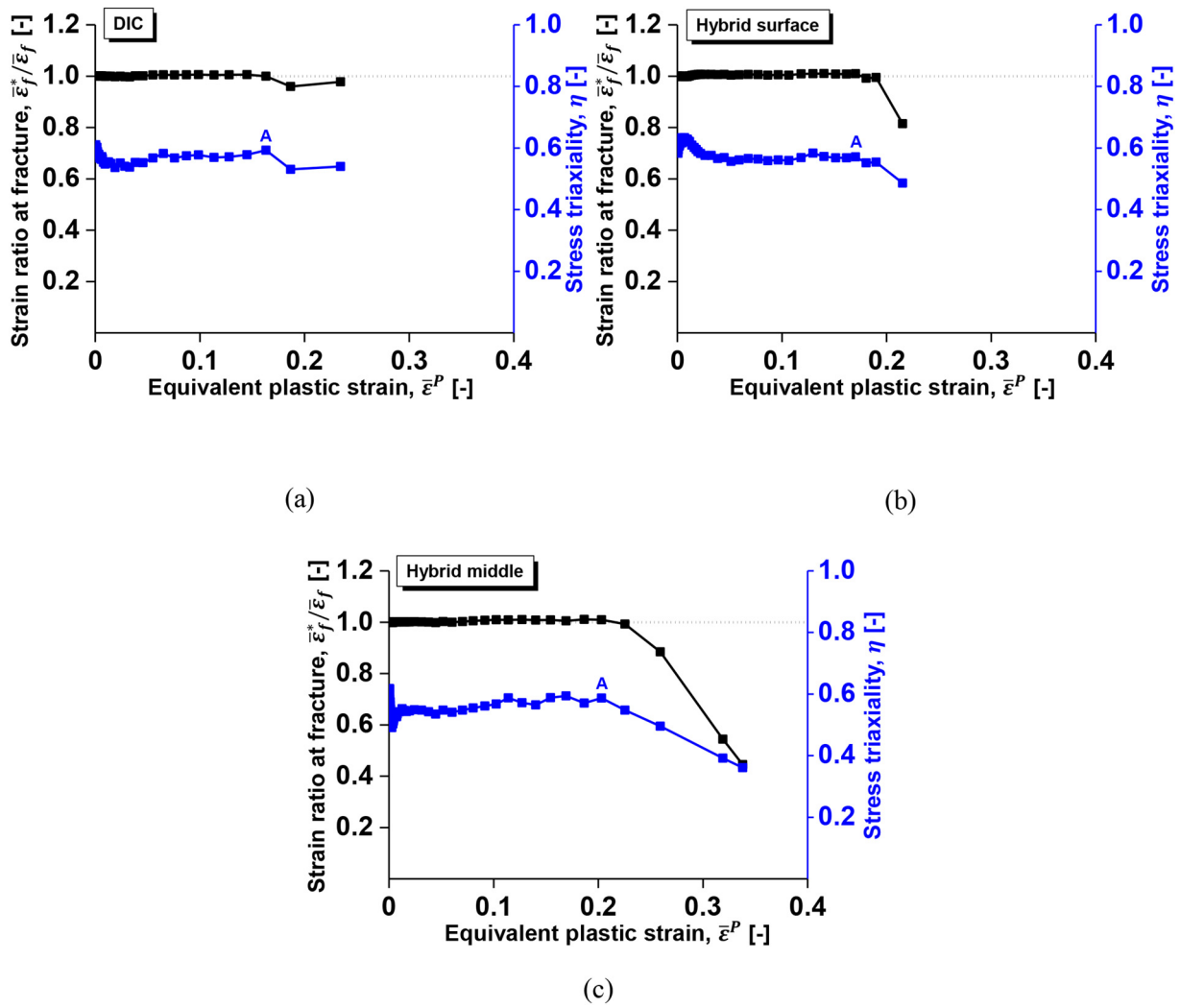
Fig. 16. Variations of the strain ratio to fracture and the stress triaxiality extracted at the element deleted at the instant of rapid loading drop for each square cup drawing simulation employing the fracture locus calibrated from: (a) the 3D-DIC analysis; and the hybrid inverse analysis using the data obtained from (b) the top and (c) the middle layers.

deformation, damage index, D, becomes $\int d\varepsilon^p / \varepsilon_f(\eta)$ so that $\overline{\varepsilon}_f^*(\eta) = \overline{\varepsilon}_f(\eta)$. In order to investigate the transition of the ductility limit, the strain at fracture was computed with respect to the loading path changes extracted from the first and last elements deleted for each simulation that employs the fracture envelopes constructed based on the 3D-DIC and the hybrid inverse analyses. Figs. 13 and 14 show not only the variation of the apparent fracture strain with the loading history but also the fracture envelope that is independent of the damage level. In these graphical representations, each location of A denotes a loading state that roughly distinguishes the change of overall tendency in the deformation rate with respect to the stress triaxiality.

For the comparison of the strain and region at fracture under proportional loading, a fracture strain ratio is derived for a certain loading state from a transformation of Eq. (11) as below:

$$\frac{\overline{\varepsilon}_f^*(\eta)}{\overline{\varepsilon}_f(\eta)} = \frac{\int d\overline{\varepsilon}^p}{\overline{\varepsilon}_f(\eta)} + (1-D) = \left(\frac{\int d\overline{\varepsilon}^p}{\overline{\varepsilon}_f(\eta)} - \int \frac{d\overline{\varepsilon}^p}{\overline{\varepsilon}_f(\eta)} \right) + 1 \qquad (12)$$

This relative ratio provides the simple dependence of fracture limit on the deformation history as represented in Figs. 15 and 16, which is solely related to the damage level and the value of stress triaxiality at the previous and current stages. Since each fracture envelop is calibrated using different data set obtained from the 3D-DIC and the hybrid inverse analyses, locations for element deletion are different from each

other although the fracture site is similar for all cases. This mainly results from the damage accumulation rate that is strongly related to each value of the model parameters and a mathematical form of the uncoupled fracture criterion as well. In other words, in the FE analyses, a different set of the model parameters will result in the variation of the damage accumulation rate that affects the instant of the stiffness loss in FE elements along the region where the fracture is expected to proceed, which ultimately leads to changes in the history of stress field during the space–time integration approximations for each FE simulation.

In the comparison of the loading state between the instant of the first occurrence and the rapid propagation of fracture, material points along the site of fracture propagation can be expected to undergo a gradual transition of the main loading state towards plane strain tension from the biaxial stress condition. Concerning the first and last elements deleted, the loading state of near plane strain tension is observed as the primary loading state until the onset of fracture is firstly visualized at the corner of square punch via the FE simulation while the biaxial stress state is mainly involved in the fracture initiation for the elements deleted along the punch radius at the rapid load drop as depicted in Figs. 15a and 16a. According to a way of calibrating the fracture locus, the prediction results are varied in terms of the maximum punch force and the punch stroke at the instant of rapid fracture propagation as represented in Fig. 17 and the comparison of the maximum punch force between the experiment and the finite element analyses is given in

(a)

(b)

(c)
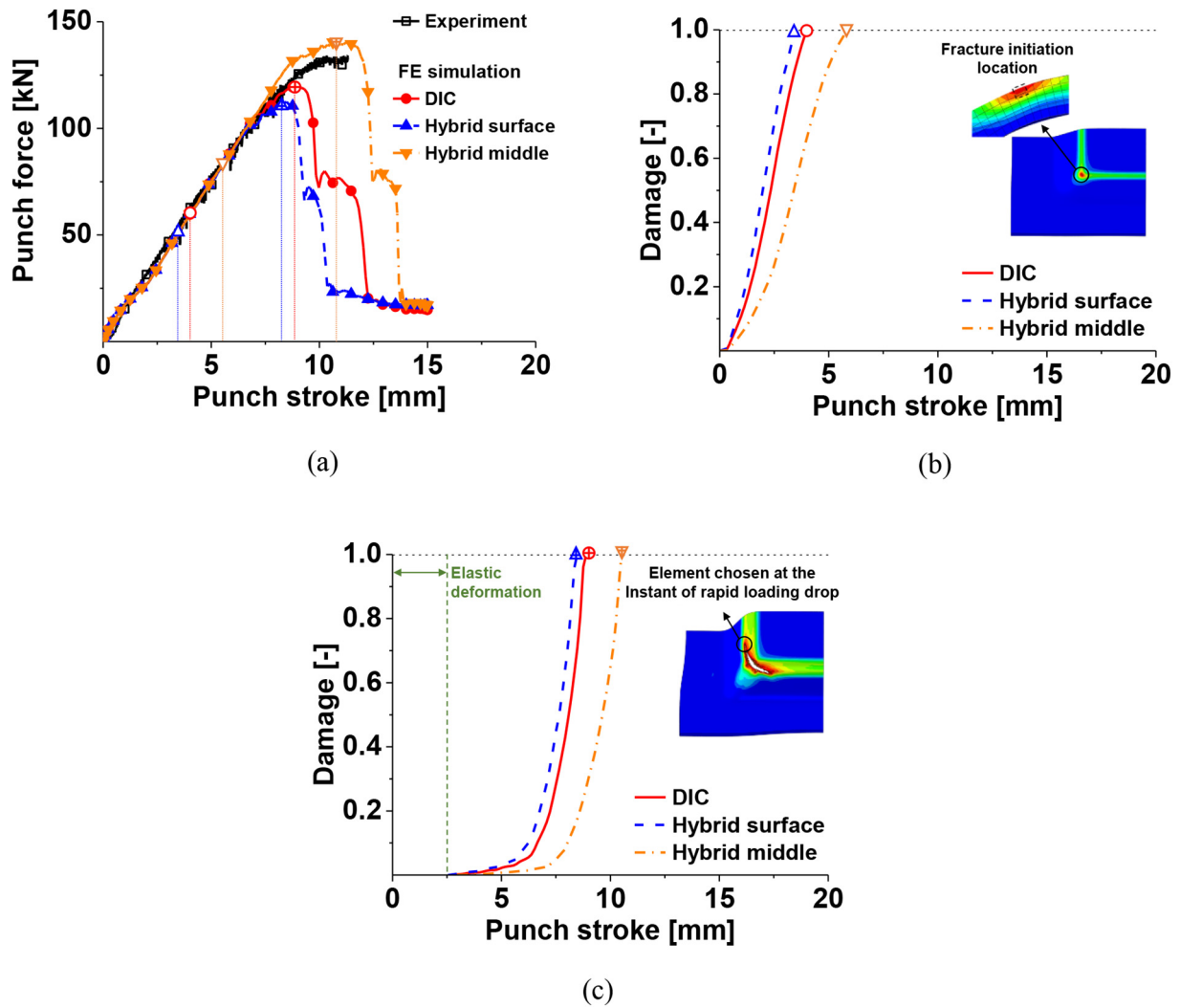
Fig. 17. Prediction of fracture initiation for the square cup deep drawing: (a) Comparison of punch force histories between the experiment and the finite element analyses; (b) Damage evolution at the element firstly deleted; and (c) Damage evolution at the element deleted at the instant of rapid loading drop.

Table 7
Comparison of the maximum punch force between the experiment and the finite element analyses.

3D-DIC analysis (on the surface of a specimen)	Hybrid inverse analysis (top layer)	Hybrid inverse analysis (middle layer)
10.32%	16.23%	4.54%

Table 7. It is noted that the damage accumulation law of $D = \int \frac{d\bar{\varepsilon}^p}{\bar{\varepsilon}_f}$ is employed in numerical analysis to assess the level of the damage during the deep drawing simulation. The best prediction on the maximum punch force is achieved for the FE analysis employing the fracture locus calibrated from the hybrid inverse analysis with the use of the data extracted from the middle layer, which represents that the level of fracture limit is solely related to the rate of damage accumulation. Particularly when the low level of fracture envelope is employed in the numerical analysis, as in the case of fracture evaluation based on the 3D-DIC and hybrid inverse analysis using the data extracted on the top layer, the loss of load-carrying capacity is accelerated especially at the deformation concentrated area. This will generate the early occurrence of the crack that rapidly propagates along the fractured surface owing to the stress concentration, which ultimately results in the underestimation of the maximum punch force. Obviously, the prediction of the instant of the fracture initiation will be a key factor considering the change of stress field, deformation mode, and damage accumulation rate that also affect the potential path of crack propagation.

6. Summary and conclusions

A comparative investigation was conducted for the numerical evaluation of the fracture limit transition according to each way of loading history and its application to the identification of the fracture envelope. From the 3D-DIC and the hybrid inverse analyses, the strain hardening at the large deformation range was obtained and successfully applied to the FE simulations for the reliable prediction of the material deformation behavior with acceptable accuracy. From the fracture tests using three different shapes of the specimens, both deformation histories and the equivalent strain were evaluated by means of the 3D-DIC analysis until the onset of fracture. The hybrid inverse analysis was subsequently performed in order to assess the strain history on the surface and middle layers, which accordingly leads to the further numerical prediction of the actual mechanical response of each sample during the deformation. By using the deformation followed by the 3D-DIC and the hybrid inverse analyses, the fracture envelopes of the DP980 1.2t steel sheet were identified based on the modified Mohr–Coulomb

fracture criterion. Three different fracture envelopes were successfully applied to the simulation of square cup deep drawing.

For the in-depth understanding of the deformation influence on the fracture limit transition, the strain at fracture was computed in consideration of the loading path change for each element deleted at the instant of not only the first occurrence but also the rapid propagation of the numerical crack. The graphical representation of the strain accompanied by the loading history allowed understanding of dynamic feature of fracture limit affected by non-proportional loading based on the mathematical foundation of linear damage accumulation when considering that the fracture envelope is basically represented under the assumption of proportional loading.

Comparison of the square cup deep drawing test and the predictions from the FE analyses confirmed that the best performance in prediction the maximum punch force is achieved with employment of the fracture envelope constructed based on the hybrid inverse analysis using the data extracted from the middle layer. It can be further expected from the simulation results that the direct application of the 3D-DIC analysis to the calibration of fracture envelope may provide reasonable predictability, especially for the case that the sheet thickness is thin enough, leading to the plane stress state that can allow avoiding the severe triaxial stress state prior to the fracture initiation.

Declaration of Competing Interest

The authors declare that they have no known competing financial interests or personal relationships that could have appeared to influence the work reported in this paper.

Acknowledgement

References

[1] R. Hill, On discontinuous plastic states, with special reference to localized necking in thin sheets, J. Mech. Phys. Solids 1 (1952) 19–30.

[2] H.W. Swift, Plastic instability under plane stress, J. Mech. Phys. Solids 1 (1952) 1–18.

[3] Z. Marciniak, K. Kuczynski, Limit strains in the processes of stretch-forming sheet metal, Int. J. Mech. Sci. 9 (1967) 609–620.

[4] S. Stören, J.R. Rice, Localized necking in thin sheets, J. Mech. Phys. Solids 23 (1975) 421–441.

[5] X. Zhu, K. Weinmann, A. Chandra, A unified bifurcation analysis of sheet metal forming limits, ASME. J. Eng. Mater. Technol. 123 (2001) 329–333.

[6] P. Hora, L. Tong, J. Reissner, A prediction method for ductile sheet metal failure in FE-simulation, Proceedings of the Numisheet'96 Conference, Dearborn, Michigan, USA 1996, pp. 252–256.

[7] S.P. Keeler, W.A. Backofen, Plastic instability and facture in sheet streched over rigid punhes, ASM Trans. Q. 56 (1964) 25–48.

[8] G. Goodwin, Application of Strain Analysis to Sheet Metal Forming Problems in the Press Shop, SAE Technical Paper 680093, 56, 1968 25–48.

[9] A.S. Argon, J. Im, R. Safoglu, Cavity formation from inclusions in ductile fracture, Metall. Trans. A. 6 (1975) 825–837.

[10] S.H. Goods, L.M. Brown, The nucleation of cavities by plastic deformation, Acta Metall. 27 (1679) 1–15.

[11] J.R. Rice, D.M. Tracey, On the ductile enlargement of voids in triaxial stress fields, J. Mech. Phys. Solids 17 (1969) 201–271.

[12] A. Weck, D.S. Wilkinson, Experimental investigation of void coalescence in metallic sheets containing laser drilled holes, Acta Mater. 56 (2008) 1774–1784.

[13] A.L. Gurson, Continuum theory of ductile rupture by void nucleation and growth: Part I: yield criteria and flow rules for porous ductile media, J. Eng. Mater. Technol. 99 (1977) 2–15.

[14] V. Tvergaard, A. Needleman, Analysis of the cup-cone fracture in a round tensile bar, Acta Metall. 32 (1984) 157–169.

[15] D. Steglich, W. Brocks, J. Heerens, T. Pardoen, Anisotropic ductile fracture of Al 2024 alloys, Eng. Fract. Mech. 75 (2008) 3692–3706.

[16] M.G. Chausov, P.O. Maruschak, A.P. Pylypenko, L. Markashova, Enhancing plasticity of high-strength titanium alloys VT 22 under impact-oscillatory loading, Philos. Mag. 97 (6) (2017) 389–399.

[17] M.G. Chausov, P.O. Maruschak, V. Hutsaylyuk, L. Śnieżek, A.P. Pylypenko, Effect of complex combined loading mode on the fracture toughness of titanium alloys, Vacuum. 147 (2018) 51–57.

[18] V. Hutsaylyuk, P. Maruschak, I. Konovalenko, S. Panin, R. Bishchak, M. Chausov, Mechanical properties of gas main steels after long-term operation and peculiarities of their fracture surface morphology, Materials 12 (3) (2019) 491.

[19] T. Sirinakorn, S. Wongwises, V. Uthaisangsuk, A study of local deformation and damage of dual phase steel, Mater. Des. 64 (2014) 729–742.

[20] T. Balan, X. Lemoine, E. Maire, A.M. Habraken, Implementation of a damage evolution law for dual-phase steels in Gurson-type models, Mater. Des. 88 (2015) 1213–1222.

[21] A.S. Khan, H. Liu, A new approach for ductile fracture prediction on Al 2024-T351 alloy, Int. J. Plast. 35 (2012) 1–12.

[22] S. Kut, The application of the formability utilization indicator for finite element modeling the ductile fracture during the material blanking process, Mater. Des. 31 (2010) 3244–3252.

[23] B. Meng, M.W. Fu, C.M. Fu, K.S. Chen, Ductile fracture and deformation behavior in progressive microforming, Mater. Des. 83 (2015) 14–25.

[24] B. Wang, Z. Liu, Evaluation on fracture locus of serrated chip generation with stress triaxiality in high speed machining of Ti6Al4V, Mater. Des. 98 (2016) 68–78.

[25] F. Šebek, J. Petruška, P. Kubík, Lode dependent plasticity coupled with nonlinear damage accumulation for ductile fracture of aluminium alloy, Mater. Des. 137 (2018) 90–107.

[26] F.A. McClintock, A criterion of ductile fracture by the growth of holes, J. Appl. Mech. 35 (1968) 363–371.

[27] G. Le Roy, J.D. Embury, G. Edwards, M.F. Ashby, A model of ductile fracture based on the nucleation and growth of voids, Acta Metall. 29 (1981) 1509–1522.

[28] M.G. Cockcroft, D.J. Latham, Ductility and the Workability of Metals, J. Inst. Met. 96 (1968) 33–39.

[29] S. Oh, C.C. Chen, S. Kobayashi, Ductile failure in axisymmetric extrusion and drawing, Part 2, Workability in extrusion and drawing, J. Eng. Ind. 101 (1979) 36–44.

[30] P. Brozzo, B. Deluca, R. Rendina, A New Method for the Prediction of Formability in Metal Sheets, Proc. of the 7th biennial Conf IDDR, 1972 9–13.

[31] M.L. Wilkins, R.D. Streit, J.E. Reaugh, Cumulative-Strain-Damage Model of Ductile Fracture: Simulation and Prediction of Engineering Fracture Tests, ucrl-53058, Technical Report, Lawrence Livermore Laboratory, Livermore, CA, 1980.

[32] I. Barsoum, J. Faleskog, Rupture mechanisms in combined tension and shear – micromechanics, Int. J. Solids Struct. 44 (2007) 5481–5498.

[33] S.S. Haltom, S. Kyriakides, K. Ravi-Chandar, Ductile failure under combined shear and tension, Int. J. Solids Struct. 50 (2013) 1507–1522.

[34] Z. Xue, J. Faleskog, J.W. Hutchinson, Tension-torsion fracture experiments – Part II: simulations with the extended Gurson model and a ductile fracture criterion based on plastic strain, Int. J. Solids Sturct. 50 (2013) 4258–4269.

[35] L. Xue, T. Wierzbicki, Ductile fracture initiation and propagation modeling using damage plasticity theory, Eng. Fract. Mech. 75 (2008) 3276–3293.

[36] Y. Bai, T. Wierzbicki, A new model of metal plasticity and fracture with pressure and Lode dependence, Int. J. Plast. 24 (2008) 1071–1096.

[37] Y. Bai, T. Wierzbicki, Application of extended Mohr-Coulomb criterion to ductile fracture, Int. J. Fract. 161 (2010) 1–20.

[38] Y. Bai, T. Wierzbicki, A comparative study of three groups of ductile fracture loci in the 3D space, Eng. Fract. Mech. 135 (2015) 147–167.

[39] Y. Jia, Y. Bai, Ductile fracture prediction for metal sheets using all-strain-based anisotropic eMMC model, Int. J. Mech. Sci. 115–116 (2016) 516–531.

[40] N. Park, H. Huh, J.B. Nam, C.G. Jung, Anisotropy effect on the fracture model of DP980 sheets considering the loading path, Int. J. Automot. Technol. 16 (1) (2015) 73–81.

[41] N. Park, H. Huh, S.J. Lim, Y. Lou, Y.S. Kang, M.H. Seo, Fracture-based forming limit criteria for anisotropic materials in sheet metal forming, Int. J. Plast. 96 (2017) 1–35.

[42] N. Park, H. Huh, J.W. Yoon, Anisotropic fracture forming limit diagram considering non-directionality of the equi-biaxial fracture strain, Int. J. Solids Struct. 151 (2018) 181–194.

[43] F. Šebek, N. Park, P. Kubík, J. Petruška, J. Zapletal, Ductile fracture predictions in small punch testing of cold-rolled aluminium alloy, Eng. Fract. Mech. 206 (2019) 509–525.

[44] Y. Bao, T. Wierzbicki, On fracture locus in the equivalent strain and stress triaxiality space, Int. J. Mech. Sci. 46 (2004) 81–98.

[45] A.M. Beese, M. Luo, Y. Li, Y. Bai, T. Wierzbicki, Partially coupled anisotropic fracture model for aluminum sheets, Eng. Fract. Mech. 77 (2010) 1128–1152.

[46] M. Dunand, D. Mohr, Hybrid experimental-numerical analysis of basic ductile fracture experiments for sheet metals, Int. J. Solids Struct. 47 (2010) 1130–1143.

[47] Y. Lou, J.W. Yoon, Anisotropic behavior in plasticity and ductile fracture of an aluminum alloy, Key Eng. Mater. 651–653 (2015) 163–168.

[48] K. Charoensuk, S. Panich, V. Uthaisangsuk, Damage initiation and fracture loci for advanced high strength steel sheets taking into account anisotropic behaviour, J. Mater. Process. Technol. 248 (2017) 218–235.

[49] Y. Lou, J.W. Yoon, Anisotropic yield function based on stress invariants for BCC and FCC metals and its extension to ductile fracture criterion, Int. J. Plast. 101 (2018) 125–155.

[50] N. Park, T.B. Stoughton, J.W. Yoon, A new approach for fracture prediction considering general anisotropy of metal sheets, Int. J. Plast. 124 (2020) 199–225.

[51] K. Chung, N. Ma, T. Park, D. Kim, D. Yoo, C. Kim, A modified damage model for advanced high strength steel sheets, Int. J. Plast. 27 (2011) 1485–1511.